J. Fluid Mech. (1991), *vol.* 229, *pp.* 269–289
Printed in Great Britain

Some observations of tip-vortex cavitation

By R. E. A. ARNDT,[1] V. H. ARAKERI[2] AND H. HIGUCHI[3]

[1] St. Anthony Falls Hydraulic Laboratory, University of Minnesota, Minneapolis, MN 55455, USA

[2] Indian Institute of Science, Bangalore, India

[3] Syracuse University, NY 13210, USA

(Received 2 July 1990 and in revised form 26 January 1991)

Cavitation has been observed in the trailing vortex system of an elliptic planform hydrofoil. A complex dependence on Reynolds number and gas content is noted at inception. Some of the observations can be related to tension effects associated with the lack of sufficiently large-sized nuclei. Inception measurements are compared with estimates of pressure in the vortex obtained from LDV measurements of velocity within the vortex. It is concluded that a complete correlation is not possible without knowledge of the fluctuating levels of pressure in tip-vortex flows. When cavitation is fully developed, the observed tip-vortex trajectory shows a surprising lack of dependence on any of the physical parameters varied, such as angle of attack, Reynolds number, cavitation number, and dissolved gas content.

1. Introduction

The present article is concerned with the problem of cavitation in the trailing vortex system of a lifting surface. In general, flows with cavitation are characterized by the cavitation number σ which is defined as

$$\sigma = \frac{p_\infty - p_v}{\frac{1}{2}\rho U_\infty^2},$$

with p_∞ and U_∞ being the free-stream pressure and velocity respectively, ρ the liquid density and p_v the vapour pressure at the bulk temperature. The magnitude of the cavitation number near the inception conditions is the cavitation inception number designated by σ_i. If one assumes cavitation occurs when the minimum pressure in the flow, p_{min}, is equal to the vapour pressure p_v, then one readily sees a connection between σ_i and $-C_{p_{min}}$ in the form

$$\sigma_i = -C_{p_{min}}.$$

Here $C_{p_{min}}$ is the minimum pressure coefficient given by

$$C_{p_{min}} = \frac{(p_{min} - p_\infty)}{\frac{1}{2}\rho U_\infty^2}.$$

One of the first exhaustive studies on cavitation produced by a vortex system from a lifting surface was due to McCormick (1962). Both analytical and experimental investigations were carried out. Particular attention was paid to predicting the conditions for cavitation onset or inception and their comparison with experimental observations on the basis of the relationship noted above. Such a comparison then requires the analytical prediction of the minimum pressure coefficient in the vortex

system. Since the vortex system downstream of a lifting surface goes through an evolutionary process, McCormick analysed a completely rolled-up vortex sheet, which is typical of the picture near the lifting surface, as one of the two limiting cases. The completely rolled-up vortex sheet was modelled according to Rankine's hypothesis, in which a vortex is assumed to be composed of a core where the vorticity is constant and outside this core the motion is taken to be irrotational. Integrating the equation of motion for such a model, see for example Batchelor (1964), the pressure coefficient at the centre of the vortex is found to depend on the core radius and local vortex strength. McCormick proceeded to compute the core radius by relating the kinetic energy of the vortex system per unit length to the induced drag of the wing which is producing the system. The strength of the vortex was related to the bound circulation at the wing mid-span. The analysis of the non-distorted vortex sheet, being the other limiting case, was done along similar lines. The predicted pressure coefficients at the centre of the vortex core in both the cases showed certain trends which were totally contrary to the experimental observations. A few of these discrepancies are listed below:

(i) predicted pressure coefficients showed a strong dependence on the aspect ratio of the wing, whereas the observed cavitation inception numbers showed hardly any dependence on the aspect ratio;

(ii) predicted pressure coefficients showed a dependence like α^2 on the angle of attack, α, whereas the observed cavitation inception numbers showed a dependence to a much lower power of α;

(iii) predictions showed the rectangular planform to be more susceptible to cavitation than the elliptic planform of the same aspect ratio, whereas the observed σ_i values for the elliptic planform were found to be higher than those for the rectangular planform.

In view of this disagreement (even qualitative) between experimental observation and the predictions based on either the rolled-up or non-distorted vortex sheet, McCormick concluded that the induced drag of a wing, contrary to the belief at the time, did not govern the size of the trailing vortex core. He then presented a semiempirical analysis where the core radius was related to the boundary-layer thickness on the pressure side of the lifting wing. In the light of more recent studies by Arndt & George (1978), Katz (1984) and Ooi (1985), who have shown a complex interaction between the pressure fields and 'nuclei' (weak spots in the liquid sample are termed nuclei) content of the liquid sample leading to cavitation inception in a certain class of flows, it may be stated that the conclusions of McCormick based on the disagreements noted may have been premature. In fact, the prediction of cavitation inception conditions in a flow field could be one of the severest tests for the ability of an analytical or numerical model's ability to predict the detailed features of such a flow field. Under certain conditions, or to be more precise, in the presence of sufficiently large-sized nuclei, cavitation inception is the most sensitive detector of the local instantaneous minimum static pressures in the flow field. In many situations, these minimum pressures are determined by local conditions and not the 'global' conditions. To cite an example, Arakeri & Acosta (1973) have shown that the cavitation inception conditions on a hemispherically nosed body are determined by the local conditions in the reattachment region of a laminar separation bubble and not by the global conditions which would relate to the minimum pressure as predicted on the basis of a potential flow computation of the flow past the body.

Therefore, even though the ultimate test of an analytical or numerical study is on

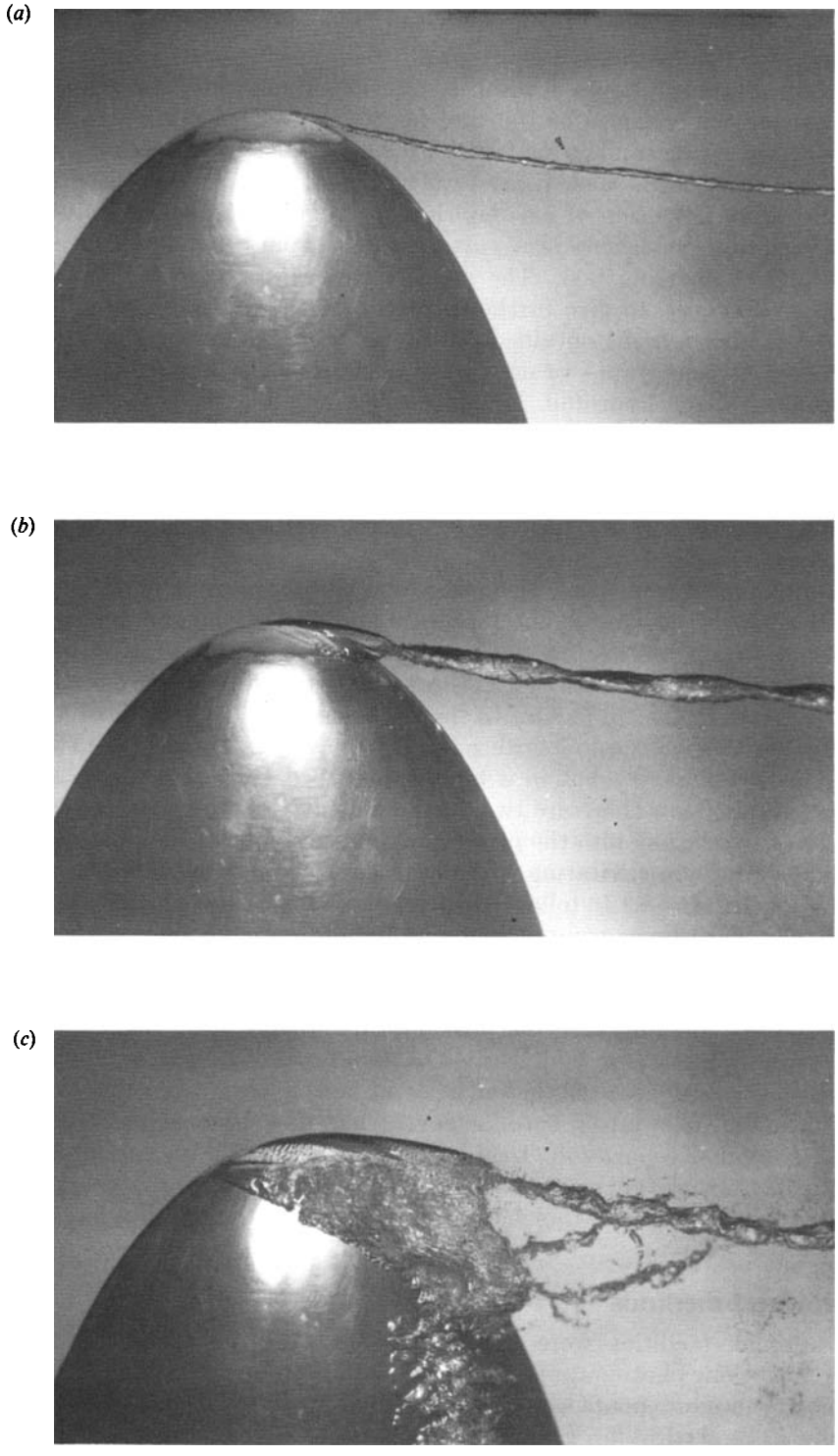

FIGURE 1. Photographs showing development of tip and other forms of cavitation on a hydrofoil. $\gamma = 4.5$ p.p.m. (*a*) Continuous tip-vortex cavity ($\sigma = 1.15$, $\alpha - \alpha_0 = 9.5°$, $Re = 5.3 \times 10^5$); (*b*) twisted tip-vortex cavity ($\sigma = 0.58$, $\alpha - \alpha_0 = 9.5°$, $Re = 5.3 \times 10^5$); (*c*) tip-vortex cavitation, secondary vortex cavitation and surface cavitation ($\sigma = 0.43$, $\alpha - \alpha_0 = 11.5°$, $Re = 5.3 \times 10^5$).

the basis of favourable comparison with experimental observations, such comparisons must be done with great caution, this being particularly so where physical understanding of the processes leading to the experimental observations are not clear. We believe the latter to be the case for the cavitation process in the vortex system of a lifting surface and present evidence here to justify this claim. This is true, in spite of several studies subsequent to McCormick's which have been primarily experimental or an extension of his empirical formulation. Therefore, prediction of cavitation inception conditions in a vortex system from a lifting surface still is a formidable and challenging task. The present studies are expected to aid in this ultimate goal. However, to give further insight into the scope of present work, we present a set of photographs obtained during the study to be described later.

Figure 1 shows photographs of developed cavitation at different stages from an elliptic planform lifting hydrofoil. In figure 1 (*a*), a well-defined tip-vortex cavity, attached to the tip, is observed. Such a cavity is highly stable both spatially and temporally and extends well into the diffuser section of the water tunnel. Since cavitation is associated with the low pressures in the tip-vortex core region, we can compare the tip-vortex cavity trajectory with the predicted location of the rolled-up vortex from numerical studies of this problem. We select the most recent results of Krasny (1987) for this purpose. It is clear from the photograph in figure 1 (*b*), that the tip-vortex cavity develops some form of instability giving the appearance of a twisted ribbon. It is interesting to speculate on the source and nature of this instability. We only have a hint that this may be associated with the initial 'twist' given to the cavity in the tip region. In the photograph of figure 1 (*c*), we have well-developed cavitation on the foil surface and in the vortex system. We still have a dominant tip-vortex cavity but in a highly disturbed state. However, unlike the earlier photographs, now there are two additional cavities emerging downstream of the tip region and merging into the primary tip-vortex cavity. The presence of these suggests that under non-cavitating conditions there are sources of relatively strong secondary vorticity. In §3.1 to follow, we present results of flow visualization studies along with boundary-layer computations to indicate the possible source of these secondary vortices. In §3.4 we also present detailed probing of the vortex system of the foil with a laser Doppler velocimeter which clearly indicates the influence of the secondary vortices merging with the primary tip vortex.

In the photograph of figure 1 (*c*), we also see two types of surface cavitation on the foil. A developed cavity near the tip and a 'band' cavity away from the tip along the spanwise direction. The latter type of cavity has now been associated with the presence of a laminar separation 'bubble' (see Arakeri 1975) and again in §3.1 we confirm this fact. However, more importantly we also examine the possible role of this separation zone on cavitation inception in the tip-vortex region in §3.2.

2. Experimental methods

Three different facilities were utilized for the present study. Detection of cavitation inception, photographic observations of the type shown in figure 1, and limited velocity measurements were made in a high-speed water tunnel facility at the St. Anthony Falls Hydraulics Laboratory (Wetzel & Killen 1982). This facility has a test section of 190 mm square cross-section with a length of 1250 mm. It is not equipped with a resorber but has an unusually large contraction ratio of ~ 100. The test body used in this facility was an elliptical planform hydrofoil having a base chord length, c_0, of 81 mm and a semispan, s, of 95 mm giving a full span aspect ratio,

A of 3. The cross-section of the hydrofoil had a NACA 66_2-415 shape with an $a = 0.8$ mean line. The design lift coefficient, all due to camber, was 0.4. Based on available aerodynamic data, the angle of zero lift, α_0, was estimated to be $-2.5°$ for the unmodified 66_2-415 shape. Similar data for the hybrid shape used in this study are not available. However, the theoretical values for the 66 series meanline and the $a = 0.8$ meanline are $\alpha_0 = -4.04°$ and $-3.03°$, respectively. Subsequent observations, using a laser sheet, to determine the angle at which the tip-vortex rotation reversed direction indicated that $\alpha_0 = -2° \pm 1°$. Abbot & von Doenhoff (1959) state the the actual magnitude of α_0 is typically 74% of the theoretical value. With this in mind, the decision was made to reference all angle-of-attack data to the original estimate of $\alpha_0 = -2.5°$.

In addition, the free-stream velocity, U_∞ and the dissolved gas content, γ were also varied. The general procedure for inception observations was as follows. At a given geometric angle of attack and free-stream velocity, the tunnel was run at high pressures (for example, pressure corresponding to a test section σ-value of 12 at U_∞ of 6.9 m/s) for 10 minutes, and then the test section pressure was slowly lowered until inception of cavitation was visually detected under the illumination of stroboscopic lighting. In a few cases the visual inception call was confirmed through acoustical monitoring and video recording. The static pressure in the test section and the contraction pressure drop were measured with the help of U-tube mercury monometers. These readings were used to compute the σ, U_∞ and other required parameter values. The mean temperature for the tests was 19.7 °C. The velocity range covered was sufficient to give a Reynolds number, Re, range of 3×10^5 to 11.5×10^5 with Re based on the free-stream velocity and c_0, the base chord length. The angle of attack $(\alpha - \alpha_0)$ was varied from 5.5° to 15.5° and three different values of air content, γ, were used, namely 12.5, 8, and 4 p.p.m. The air content of the tunnel water was monitored with the help of a VanSlyke apparatus.

The bulk of the velocity surveys in the tip-vortex region were made using another recirculating water tunnel having the same test section dimension as the facility used for cavitation studies. This facility was preferred since it was modified with optical-quality glass walls. Straub, Ripken & Olson (1955) describe this low-speed water tunnel in detail. The test model was the same foil used for the cavitation studies, as described earlier. A custom designed laser Doppler anemometer (LDA) system was used. The system consists of optics manufactured by OEI in West Germany, a Spectra Physics 3 W argon ion laser and signal processing equipment manufactured by TSI in the USA. The system was operated in the backscatter mode. Two green beams measured tangential or vertical components, whereas two blue beams were used to measure the axial or horizontal velocity. All four beams were frequency shifted with four Bragg cells operating near 40 MHz. These were adjusted to produce a difference frequency of 1–3 MHz. The photomultiplier outputs were processed with counters that were directly linked to an IBM AT microcomputer. There were 250–500 readings averaged at each point. The entire system was mounted on a machinist's mill fitted with optical position encoders. Spatial resolution was estimated to be 0.16 mm in width and 1.7 mm in length.

Additional velocity measurements were made in the same tunnel used for cavitation studies. For this purpose, a single-component LDA was operated in the forwardscatter mode. The light source was a 5 mW helium-neon laser. A 250 mm transmitting lens with a 3.75× beam expander provided a system with adequate spatial resolution. A single Bragg cell and mixer system were used for frequency shifting. A TSI tracker was used for processing the signal, the output of which was

analysed on-line with an HP 9836A microcomputer. This system had an improved spatial resolution of 0.07 mm in width and 0.75 mm in length. Both laser systems utilized beam expanders to achieve acceptable spatial resolution.

Axial and tangential velocity components were measured across the vortex at different downstream locations. The traverses were carried out in planes perpendicular to the vortex axis, that is along the direction normal to the wing span.

Surface oil-flow visualization studies were conducted in air to investigate the behaviour of the foil boundary layer. These were carried out in a low-speed open-circuit wind tunnel with a 43.2×30.5 cm test section, and at free-stream velocities which could be varied from 18 to 70 m/s. The test model used here was of the same geometry as the one used for cavitation studies but was of a larger size. The base chord of this model was 129.4 mm, thus giving a maximum Reynolds number of 5.3×10^5. A mixture of a light mineral oil and titanium dioxide was used as the flow tracer.

3. Results and discussion

3.1. *Real flow characteristics of the foil*

A photograph of the observed surface flow pattern from the wind tunnel flow visualization studies is shown in figure 2(*a*) and some features can be pointed out here. There is a clear line indicating flow separation near about 60% of the local chord along the spanwise direction. The flow reattaches to form a well-defined 'laminar separation bubble' except near the tip region where the topology of the flow field is not clearly defined. A few streaks downstream of reattachment seem to show flow direction away from the tip. As described in Higuchi, Quadrelli & Farell (1987), the viscous flow field showed similar characteristics at other Reynolds numbers and effective angles of attack in the range $2.5° < (\alpha - \alpha_0) < 11°$. Above an effective angle of attack of approximately $\alpha - \alpha_0 = 11.5°$, the viscous flow field varied considerably with both angle of attack and Reynolds number. For example, at an effective angle of attack of 12.5°, significant changes in the flow field are observed as the Reynolds number is varied from 2.7×10^5 to 5.3×10^5 as shown in figure 3. A variety of combinations of leading-edge separation and turbulent trailing-edge separation are observed at angles of attack greater than 12.5° in the range of Reynolds number 2.7×10^5 to 5.3×10^5. Stall was observed at an effective angle of attack of 22.5° at a Reynolds number of 2.7×10^5.

For $(\alpha - \alpha_0)$ less than 11.5°, the gross features of the observed viscous flow can be predicted on the basis of simple boundary-layer computations as described below. These computations were based on assuming the flow field to be locally two-dimensional and hence are not likely to be accurate near the tip region. The theoretical pressure distribution at a given angle of attack was computed using the method described in Abbot & von Doenhoff (1959). The boundary-layer growth calculations were made using the Thwaites method, and the separation bubble, if existing, was assumed to be either short or long based on the results of Gaster (1967). In addition, boundary-layer stability estimates were made to examine whether transition would occur within the attached boundary layer at various Reynolds numbers. The flat-plate results of Wazzan, Okamura & Smith (1968) were used since the pressure distribution showed a flat region from almost 5% chord to 60% chord, the location of the minimum pressure point. Using the maximum spatial amplification factor for the flat plate and with the e^9 criterion for transition (as discussed in Smith & Gamberoni 1956), it was predicted that laminar separation

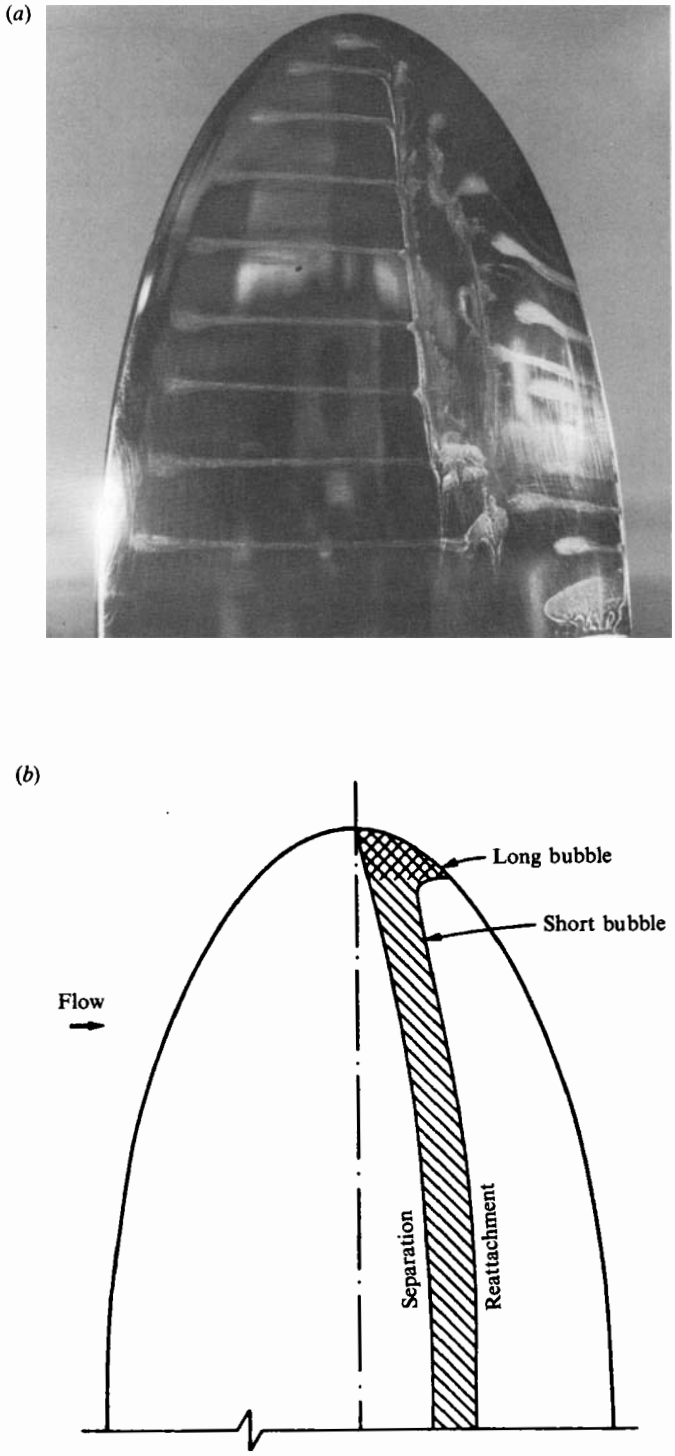

FIGURE 2. Real fluid flow characteristics of the hydrofoil on the suction side with $\alpha - \alpha_0 = 7.5°$ and $Re = 5.3 \times 10^5$; (*a*) the observed surface flow pattern in a wind tunnel; (*b*) predicted flow pattern.

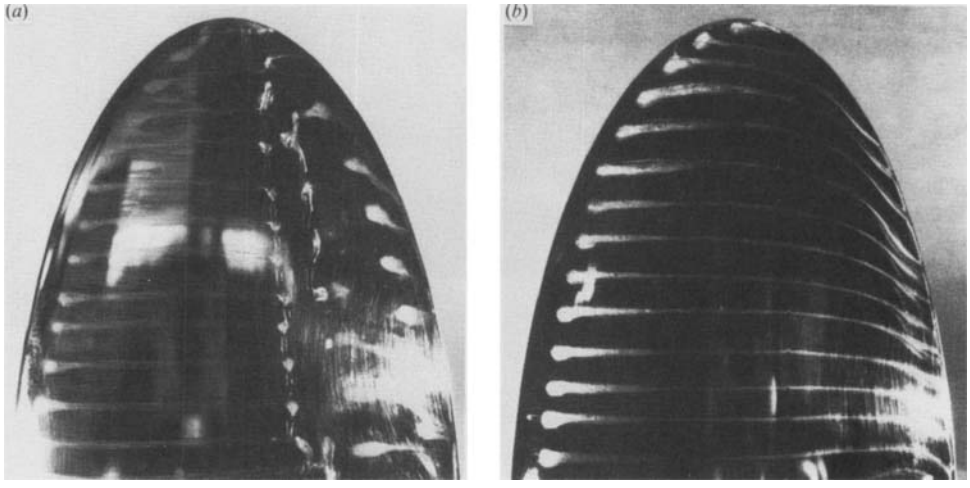

FIGURE 3. Photographs of the observed surface flow pattern at $(\alpha-\alpha_0) = 12.5°$: (a) $Re = 2.7 \times 10^5$; (b) $Re = 5.3 \times 10^5$.

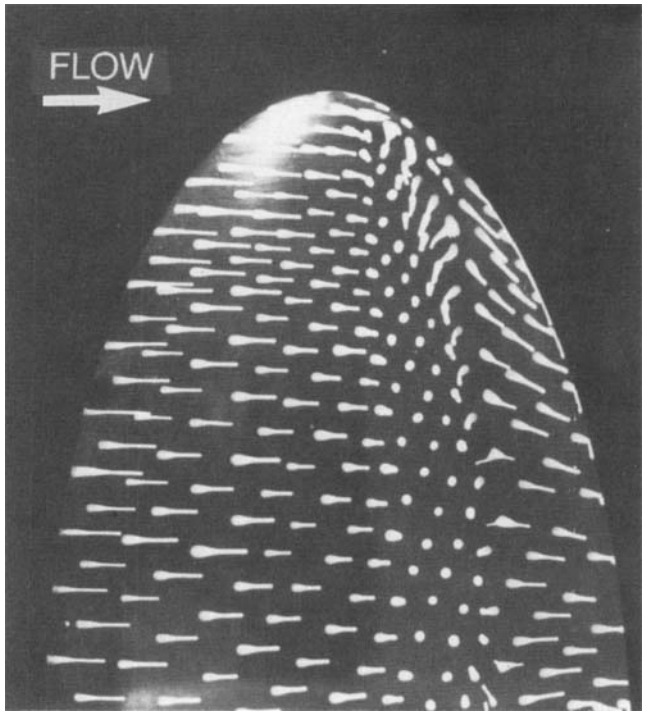

FIGURE 4. A photograph of the observed detailed surface flow pattern on the suction side with $\alpha-\alpha_0 = 7.5°$ and $Re = 5.3 \times 10^5$.

would prevail up to an Re value of about 2×10^6. In the past, these simple methods of boundary-layer computations have shown remarkably good agreement with observations on axisymmetric bodies (Arakeri & Acosta 1973; Arakeri 1974).

One set of computed results of the real flow field on the suction side of the foil at $(\alpha-\alpha_0) = 7.5^0$ and $Re = 5.3 \times 10^5$ is shown in figure 2(b). A laminar separation bubble

FIGURE 5. A photograph of tip-vortex cavitation inception. ($\sigma = 1.4$, $\alpha - \alpha_0 = 2.4°$, $Re = 6.1 \times 10^5$.) Note the total absence of cavitation on the foil.

is predicted as indicated. Since the local-chord Reynolds number on an elliptic planform decreases towards the tip, an inherently three-dimensional reattachment pattern is generated. A short separation bubble is predicted to extend almost to the tip, and a long bubble is predicted in the tip region. It is a very likely that the varying separation bubble length will set up spanwise pressure gradients, thus influencing the real flow field near the tip. This, in fact, is very much suggested by the more detailed surface flow pattern observed in the tip area of the photograph of figure 4. However, there is a more fundamental issue involved here, which we consider next.

We expect some vorticity associated with the short separation bubble whose magnitude is likely to be quite different from that associated with the long separation bubble. This follows from the entirely different flow characteristics of the two separation zones as investigated by Gaster (1967). The expected difference in the vorticity and corresponding circulation must then be shed as a streamwise vortex downstream which could interact with the developing primary tip vortex. The location of the shedding of this secondary vortex would be the position near the tip where the short bubble ceases to exist. The possible existence of two such secondary vortices appears from the photograph of developed cavitation on the foil and is illustrated in figure 1 (*c*). We attribute the sources of these to the varying separation bubble lengths on both the suction and pressure sides of the foil. We next examine the potential role of the existence of the separation bubble on the foil surface on the tip-vortex cavitation inception characteristics of the foil.

3.2. *Tip-vortex cavitation inception*

As noted earlier, tip-vortex cavitation inception was detected visually under the illumination of stroboscopic lighting. There was a clearly audible intermittent hissing sound when inception took place. A photograph of tip-vortex cavitation at inception conditions is shown in figure 5. It can be observed that cavitation is localized and to obtain a clear attached cavity of the type observed in figure 1 (*a*), the cavitation number had to be lowered well below the inception value, σ_i. For example, for the

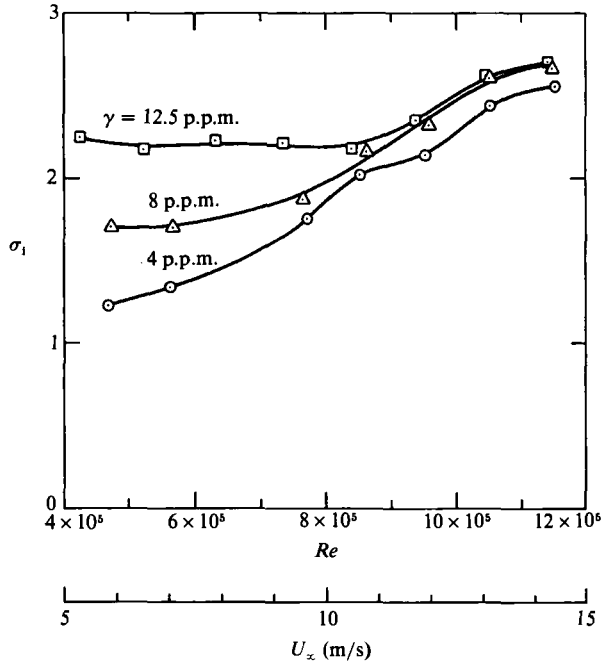

FIGURE 6. σ_i dependence on Re and with $\alpha-\alpha_0 = 8.5°$.

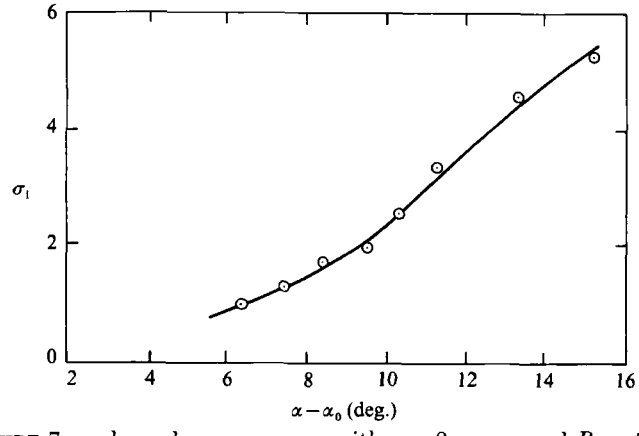

FIGURE 7. σ_i dependence on $\alpha-\alpha_0$ with γ = 8 p.p.m. and $Re = 5.58 \times 10^5$.

conditions of figure 1(*a*), σ is 1.15 and the σ_i value is close to 2. The fact that the cavitation is localized at inception and does not occur simultaneously within the entire tip-vortex core suggests the existence of axial pressure gradients in the core as analysed by Batchelor (1964). An attempt has been made by Higuchi, Arndt & Rogers (1989*b*) to locate the localized zones of inception using multiple acoustic sensors. It should be pointed out that at higher angles of attack and for particularly low air content values, the inception was in the form of a well-developed tip-vortex cavity which appeared quite suddenly. It was not possible to photograph the localized events like those shown in the photograph of figure 5.

The dependence of σ_i on various parameters like Re, γ and $(\alpha-\alpha_0)$ is shown in figures 6 and 7. It may be noted that since a well-defined procedure was followed for inception observations, there was good repeatability. For example, in figure 6, the

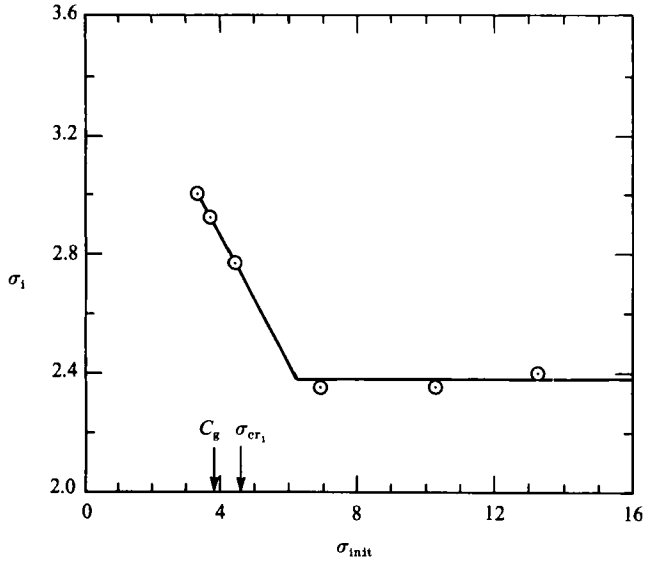

FIGURE 8. σ_i dependence on initial pressurization with $\alpha-\alpha_0 = 8.5°$. $\gamma = 12.5$ p.p.m. and $Re = 5.36 \times 10^5$.

dependence of σ_i on γ is quite consistent and no crisscrossing of the curves is observed. The σ_i values for different air content values were obtained on different days and sometimes with a considerable lapse of time. With reference to the dependence of σ_i on the angle of attack $(\alpha-\alpha_0)$ shown in figure 7 we need only note that at higher angles, σ_i seems to vary linearly with changes in $(\alpha-\alpha_0)$, whereas at lower angles, it shows a nonlinear dependence. The important point is that the variation with $(\alpha-\alpha_0)$ is quite complex. Assuming the strength of the vortex to vary linearly with $(\alpha-\alpha_0)$ would imply a variation in σ_i with $(\alpha-\alpha_0)^2$. This expected parabolic variation does not fit the data. The variation of σ_i with Re as observed in figure 6 needs further analysis. If we consider the results associated with $\gamma =$ 4.0 p.p.m., there is a consistent increase in the σ_i values for $Re > 5 \times 10^5$. As it has been done previously, if we associate a σ_i value with $-C_{p_{min}}$, then we may conclude that the $-C_{p_{min}}$ value is also Reynolds-number dependent and increases with increase in Re. However, then we have to explain why the σ_i values at higher gas content are higher than $-C_{p_{min}}$. This is possible only if the observed cavitation at inception is gaseous, which in the present case it is not, since audible sound was associated with inception which is typical of vaporous cavitation inception. Therefore, on the whole we cannot associate the observed σ_i values with the corresponding $-C_{p_{min}}$ value in the tip vortex. As pointed out earlier, this correspondence is assured only if there is a supply of sufficiently large-sized nuclei in the potential zones of cavitation.

Since in the present experiments there was no provision for artificially seeding nuclei, the only method available to potentially increase the supply of nuclei was to start with lower and lower initial excess pressure before commencing the inception observations. The results of such an exercise are shown in figure 8, where the observed σ_i is plotted against σ_{init}. Here, σ_{init} is defined as $(p_{init}-p_\infty)/\frac{1}{2}\rho U_\infty^2$, where p_{init} is the test section pressure which was held initially for about 10 minutes before the inception observations were commenced by lowering the test section pressure below p_{init}. From figure 8, it is clear that the σ_i value remains constant above a

certain value of σ_{init}, below which it starts to increase. The limiting value of σ_i is 3.0, and all the σ_i values of figure 6 are below this magnitude. Therefore, the complex dependence of σ_i on Re and γ observed in figure 6, can indeed, be partially related to the conditions for nuclei supply in the tip vortex. At high initial tunnel pressures with p_{init} well above the value of $p_{sat} = \beta\gamma$, where β is the Henry's constant and p_{sat} is the saturation pressure, we expect the nuclei content to be determined by some equilibrium mechanism which has not been fully understood. The nuclei sizes are expected to be quite small and potential for their growth will exist only when pressures are lowered such that locally $p < p_{sat}$ is satisfied. It should be noted that Arndt & Keller (1976) noted a similar trend for the volume of free nuclei, measured with a laser scattering technique, as a function of saturation level in a water tunnel. When the test section pressure was held at levels greater than the saturation level the volume of free nuclei was constant. When the test section pressure was reduced below the saturation value, the volume of free gas increased markedly. However, since gaseous diffusion is a slow process (Epstein & Plesset 1950) this must happen in regions of flow where relatively long residence times of the order of 0.1 s are possible. One of the first potential zones for this to occur is the short laminar separation zone on the suction side of the foil. Therefore, if the critical condition for the nuclei supply in this zone is taken to be the static pressure

$$p_s = p_{sat} = \beta\gamma$$

then

$$\sigma_{cr1} = \frac{\beta\gamma}{\frac{1}{2}\rho U_\infty^2} - C_{p_s}.$$

Here, σ_{cr1} is the value of σ where the above-noted condition is satisfied and C_{p_s} is the pressure coefficient, $C_{p_s} = (p_s - p_\infty)/\frac{1}{2}\rho U^2$ with p_s being the static pressure in the separation zone. Introducing the gas content coefficient, $C_g = \beta\gamma/\frac{1}{2}\rho U_\infty^2$ we can express σ_{cr1} as

$$\sigma_{cr1} = C_g - C_{p_s}.$$

With laminar boundary-layer computations, the magnitude of C_{p_s} at an angle of attack of 8.5° was estimated to be -0.75 and thus for these conditions,

$$\sigma_{cr1} = C_g + 0.75.$$

This value is shown in figure 8.

In figure 9 we show the dependence of σ_{cr1} on Reynolds number (strictly speaking through velocity variation as also depicted) along with the observed σ_i data for $\gamma =$ 4 p.p.m. and $\alpha - \alpha_0 = 8.5°$.

For σ values greater than σ_{cr1}, there is no region either on the foil or in the tunnel other than the core of the vortex where local mean static pressures are less than p_{sat} corresponding to this air content value, i.e. the liquid is subsaturated and gas nuclei do not grow. If we denote this as a nuclei starved region, then σ_i shows a strong dependence on either velocity or Re in this region. As indicated in Arakeri, Higuchi & Arndt (1986), this was found to be the case at other gas content values as well.

It is well recognized that with sufficiently small-sized nuclei, actual tensions are required to initiate cavitation. As indicated in Knapp, Daily & Hammitt (1970) the non-dimensional tension, $\Delta\sigma$, required for a bubble of radius R_0 is

$$\Delta\sigma = \frac{4}{3}\frac{T}{R_0 \frac{1}{2}\rho U_\infty^2},$$

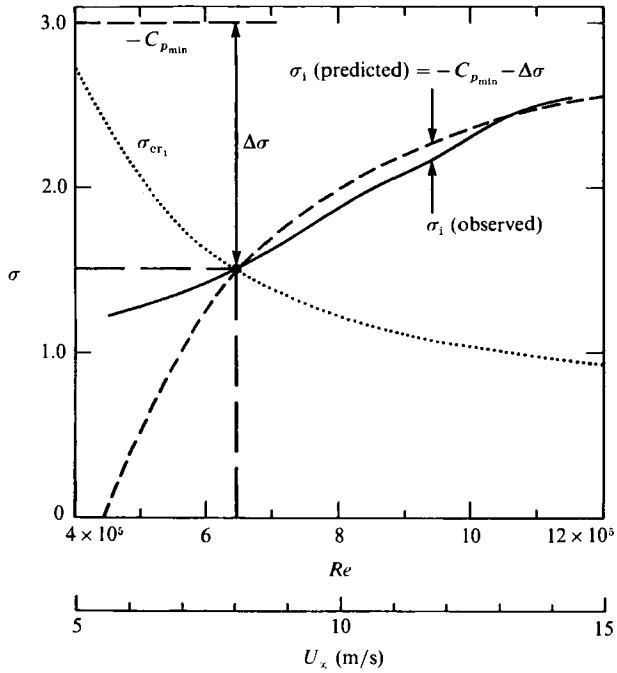

FIGURE 9. Illustration of conditions used for estimating dominant nuclei size and a comparison between the predicted and observed behaviour of σ_i. $\alpha - \alpha_0 = 8.5°$, $\gamma = 4.0$ p.p.m.

with T being the coefficient of surface tension. Therefore, the general relationship between $-C_{p_{min}}$ and σ_i can be expressed as

$$\sigma_i = -C_{p_{min}} - \Delta\sigma.$$

It is significant to note that $\Delta\sigma$ is small if R_0 is large for a given U_∞ or if U_∞ is large for a given R_0, and we expect $\sigma_i \to -C_{p_{min}}$ under these conditions. We can use the above expressions to estimate the dominant size of nuclei, by measuring σ_i and inferring $-C_{p_{min}}$ by some technique. Such an estimation was done by making the following assumptions:

(i) the limiting value of σ_i in figure 8 is the magnitude of $-C_{p_{min}}$ and we take $-C_{p_{min}} = 3.0$;

(ii) the dominant nuclei size R_0 is associated with the conditions at the crossing point of σ_i and σ_{cr1}. Any point beyond the crossing could also have been chosen.

With the help of figure 9, the estimated value of the dominant nuclei size, R_0, turns out to be 1.9 μm. If we further assume that R_0 and $-C_{p_{min}}$ remain constant, that is independent of Reynolds number, then the predicted behaviour of σ_i is as shown in figure 9. The predicted trend compares very favourably with the observed trend in the nuclei-starved region. The point we want to emphasize is that the observed variation in σ_i with Reynolds number is not a reflection of the $-C_{p_{min}}$ dependence on Reynolds number, but is primarily controlled by nuclei content. There is some evidence that the separation zones on the foil play a role in the supply of nuclei.

3.3. *Tip-vortex cavity trajectory*

In figure 10, we present measurements of the tip-vortex cavity trajectory from photographs of the type in figure 1 (*a*). The cross-hatched region indicates the extent of variation of the trajectory for differing physical parameters. For x/c_0 less than 1,

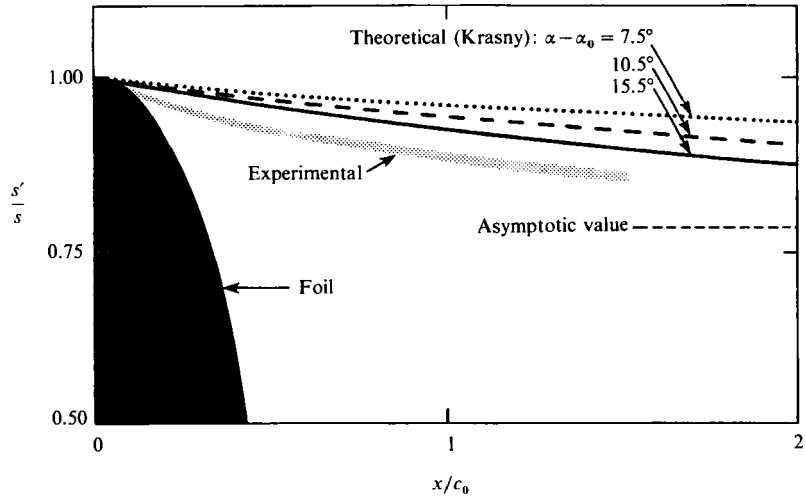

FIGURE 10. Observed tip-vortex cavity trajectory. Also shown are theoretically predicted trajectories under non-cavitating conditions.

the $(\alpha-\alpha_0)$ range covered is 5.5° to 15.5°, the Re range is from 5.3×10^5 to 10.4×10^5, the γ range is from 4.0 to 12.6 p.p.m., and the σ range is from 0.26 to 3.19. For x/c_0 greater than 1, the trajectories correspond to an Re value of 10.4×10^5, an $(\alpha-\alpha_0)$ value of 8.5° and $\gamma = 12.5$ p.p.m.; however, the σ value varied from 0.655 to 1.31, corresponding to core cavity radii values of 2.6 to 0.79 mm, respectively. The observed small spread in the trajectories indicates that the trajectory does not depend strongly on any of the parameters varied. In particular, the fact that the trajectory does not depend on σ means that we could take the tip-vortex trajectory under non-cavitating conditions to be the same as that observed under cavitating conditions†. We use this basis to make some comparisons of the predicted tip-vortex trajectory from numerical computations with those obtained experimentally.

Numerical computation of vortex sheet roll-up has been an important problem in aerodynamics and the most recent efforts in this direction are those due to Krasny (1987). The actual physical phenomena are quite complex and simplifying assumptions are invariably made in the numerical modelling. A typically used model is one in which the shed vorticity in the wake of the foil is replaced by a vortex sheet. A further simplification is to replace the spatial coordinate of the wing's line of motion by a time coordinate. This changes the steady three-space-dimensional free-boundary-value problem into an initial-value problem for the vortex sheet's evolution as a curve in two space dimensions. The physical process by which vorticity enters the wake at the wing's trailing edge is accounted for by specifying an initial spanwise circulation distribution along the vortex sheet, corresponding to a particular loading on the wing. Strictly speaking, as pointed out by Batchelor (1964), the model is only likely to be accurate in describing the features of the roll-up process far downstream of the wing trailing edge. Therefore, we may not expect

† There is some ambiguity as to what exactly the tip-vortex cavity trajectory represents; for example, is it the end point of the non-cavitating rolled-up vortex sheet or some other location like the position of 'maximum' vorticity. We suspect it is the latter. These issues were raised by Dr R. Krasny in a personal communication to one of the authors (V. H. A.). He also points out that the position of maximum vorticity (as defined in equation (9) of Krasny 1987) does not correspond to the end point of the rolled-up vortex; however, the maximum difference is quoted to be only of the order of 2%.

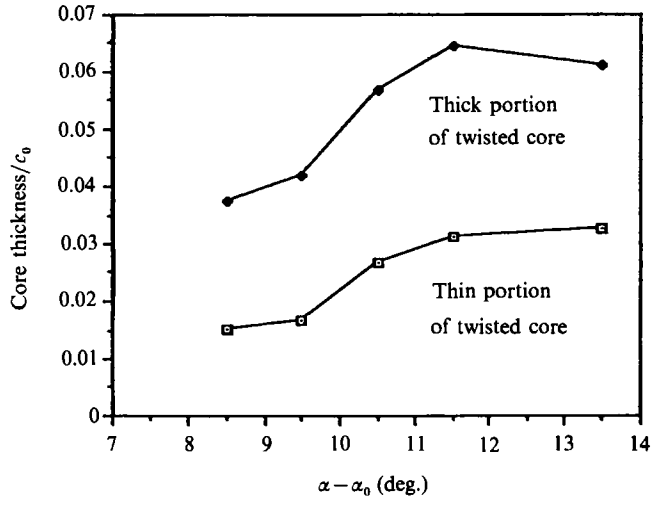

FIGURE 11. Observed dimensions of twisted cavity.

quantitative agreement between the numerical predictions and the experimental observations which are limited to the near-field of the wing, but the qualitative disagreement that the trajectory is essentially independent of the loading, as shown in figure 10, is interesting and puzzling. For the comparison noted, the non-dimensional time t^* of Krasny's figure 2 was related to the wing parameters by

$$t^* = \tfrac{1}{2}B_1 U_\infty t/s,$$

with

$$B_1 = \frac{(\alpha-\alpha_0)\tfrac{1}{2}ac_0}{[1+(ac_0/8s)]}.$$

Here, t is the actual time, s the semispan (95 mm in the present case), c_0 the base chord (81 mm in the present case) and a was taken to be 2π. By replacing U_∞ t with x, the distance downstream of the wing, we get

$$t^* = 0.0119(\alpha-\alpha_0)(x/c_0),$$

where $(\alpha-\alpha_0)$ is in degrees. A more realistic value for a would not have altered the qualitative behaviour of the curves. It should be noted that the maximum value of t^* in the present case was limited to 0.37. Therefore, on the one hand, the numerical computations clearly predict a dependence of the vortex-sheet tip trajectory on the loading, whereas the experimental observations do not show this. In assessing the quantitative and qualitative differences in figure 10, it should be noted that the present wing has a moderate aspect ratio and we are totally unaware of the role of secondary vortices in the roll-up process. In addition, whether loading remains elliptical in the presence of complex real fluid flow features described earlier is an open question.

At lower cavitation number, more fully developed cavitation occurs, as shown in figure 1(*b*). The cavitating core changes remarkably in appearance, from a thin circular region to a braided structure. Observations of the non-cavitating vortex with laser sheet illumination indicated that this braided structure also occurs in single-phase flow. Therefore, it was concluded that this structure is not due to an instability of the cavity surface as observed by Manuel, Crespo & Castro (1987), but instead is due to the interaction of a pair of corotating vortices.

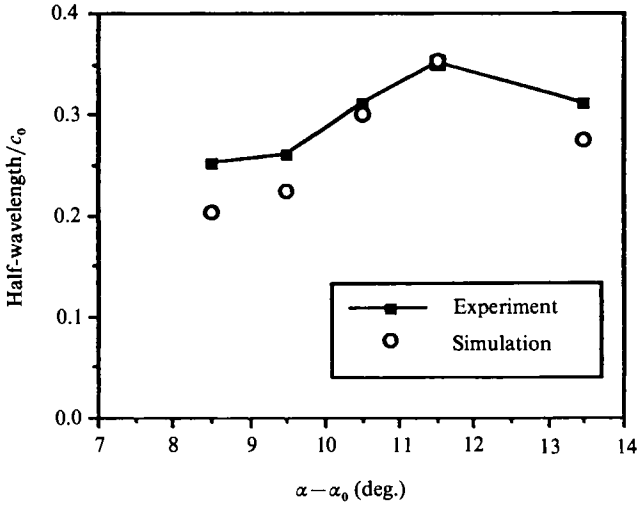

FIGURE 12. Wavelength of twisted cavity and comparison with results of numerical simulation.

Surface flow visualization also indicated that a highly three-dimensional flow structure existed in a separation bubble on the suction side of the hydrofoil. The flow near the tip is believed to be the source of a secondary vortex that becomes entwined with the primary tip vortex. Higuchi *et al.* (1989*a*) performed a simple numerical simulation to test this theory. Using the thin-layer approximation, the flow was approximated by a time-dependent, two-dimensional flow in the Trefftz plane. Here, the individual vortices were mathematically modelled by a vortex blob as used in Spalart & Leonard (1981). The relative vortex strength, core size and position of the twin vortices were varied in the simulation. Further information, useful in the simulation, was obtained from the photographic data. The wavelengths and cross-sectional dimensions of the cavity were found to be sensitive to angle of attack, as shown in figures 11 and 12. Unfortunately, there are no data available for the velocity distribution in the vicinity of the core. There is no way of knowing how the single-phase results for the twin-vortex flow simulation are modified by cavitation. Hence any comparison between the numerical simulation for single-phase flow and the observed cavity geometry is qualitative at best. (A simple, analytic form of the velocity profile in the region of an axisymmetric fully cavitated core was assumed in an earlier paper (Arakeri, Higuchi & Arndt 1988).) By assuming that the thickest portion of the fully cavitated core represents the separation distance between the two vortices in the single-phase flow simulation, Higuchi *et al.* were able to obtain good agreement between the calculated and observed wavelengths as shown in figure 12. It is of interest to note that a similar braided structure is noted in the numerical simulations of Nuhait & Mook (1988).

3.4. *Velocity and pressure*

Figures 13–15 contain samples of the velocity data obtained in this study. Figure 13 presents measurements of vertical velocities, w, in the tip vortex made at two axial positions in the vortex at a Reynolds number of 5.2×10^5 and $(\alpha-\alpha_0) = 12°$, using the single-component LDA. The data are shown on an expanded scale to illustrate that the vortex appears to be well developed by $x/c_0 = 1$. On these and subsequent plots, y is the distance normal to both the free-stream direction and the axis of the hydrofoil. Positive values of y correspond to the suction side and negative values

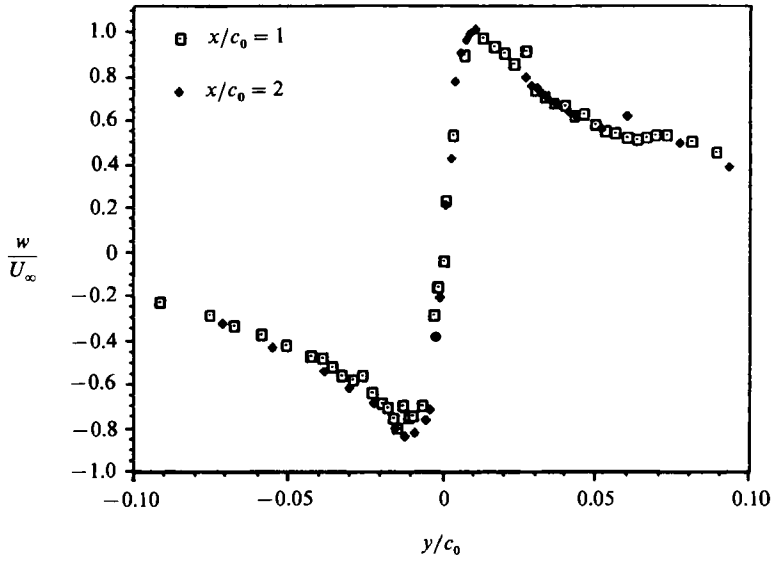

FIGURE 13. Measured velocity profiles in the cavitation water tunnel. $Re = 5.2 \times 10^5$, $\alpha - \alpha_0 = 12°$.

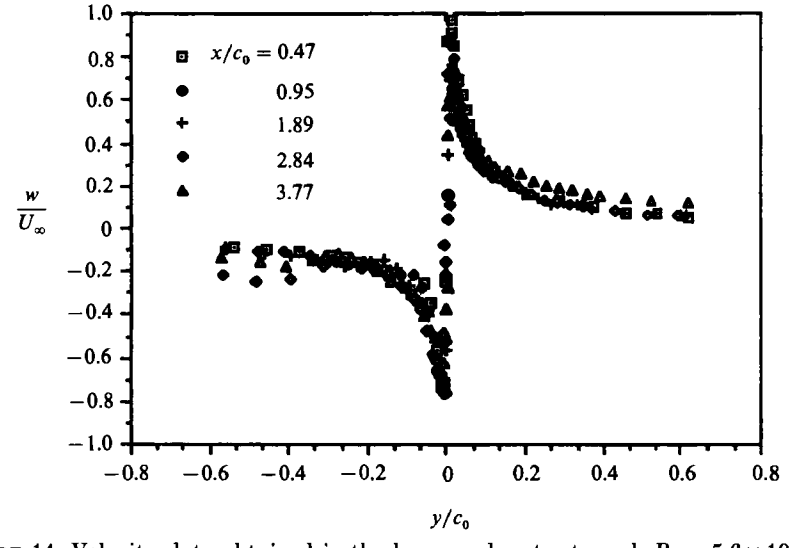

FIGURE 14. Velocity data obtained in the low-speed water tunnel. $Re = 5.6 \times 10^5$, $\alpha - \alpha_0 = 12°$.

correspond to the pressure side of the hydrofoil. It is evident from figure 13 that satisfactory resolution of the core region was achieved. It is interesting to note that the combination of small core radius (of the order 0.7 mm) and the high tangential velocity corresponds to a core rotation of approximately 96000 r.p.m. At the higher Reynolds numbers in this study, the core rotation could be as high as 220000 r.p.m.

Figure 14 contains velocity data obtained over a relatively wide range of axial positions. These data were obtained in the low-speed water tunnel with the two-component LDA at a Reynolds number of 5.6×10^5 and $(\alpha - \alpha_0) = 12°$. A comparison of the data in figures 13 and 14 indicates that very good agreement was obtained for the velocity field measured in two different facilities. The important point is that at

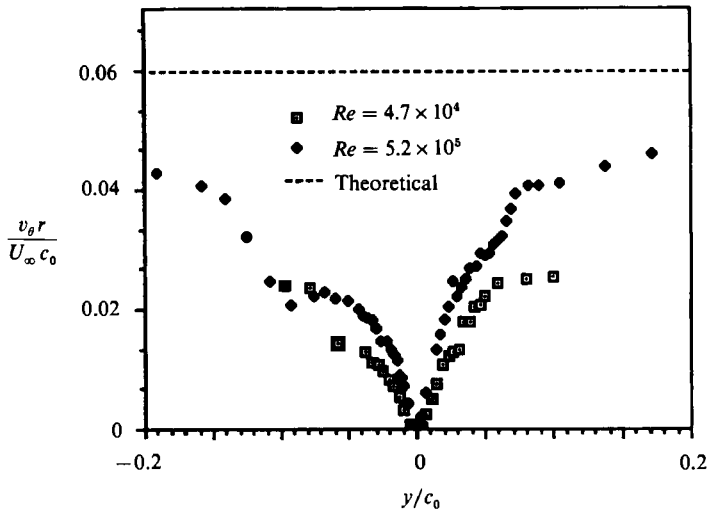

FIGURE 15. Distribution of angular momentum in the tip vortex. $x/c_0 \approx 1$.

this Reynolds number, the vortex is tightly rolled up at a relatively short distance from the hydrofoil. This is in sharp contrast to the observations of Higuchi *et al.* (1987) of the same vortex structure at much lower Reynolds number. Again, this has implications for cavitation scaling. This is illustrated in more detail in figure 15 which is a plot of the product of radius and tangential velocity. The integral of this parameter over all angular positions is the circulation:

$$\Gamma = \int_0^{2\pi} r v_\theta \, \mathrm{d}\theta,$$

where $v_\theta = |w|$. The differences in the distribution of angular momentum per unit mass with radius between the suction side and the pressure side are a reflection of the measured asymmetry of the vortex. It would be expected that the actual circulation distribution would be approximately equal to the average of the rv_θ distribution measured on either side of the foil. Unfortunately v_θ would have to be measured at all angular positions as well as at all radii to obtain the exact value of the circulation distribution. Therefore, the total circulation at any radial position can only be inferred from this plot. It is important to note that at lower Reynolds number, the total circulation is a small fraction of the theoretical value for a fully rolled-up vortex. At higher Reynolds number, the total circulation is higher, and more closely approaches the theoretical value. The differences in total circulation could be due to Reynolds scaling of both vortex roll-up and lift (which determines the total circulation). Unfortunately the total lift was not measured. However, it is believed that Reynolds-number effects on the total lift are relatively small. The details are given in Higuchi *et al.* (1987). Therefore, it can be concluded that there is a strong viscous effect on the vortex roll-up process.

Making boundary-layer types of approximations, the pressure field in a steady axisymmetric flow of a trailing vortex can be related to the tangential velocity, v_θ in the form (Batchelor 1964)

$$\frac{1}{\rho}\frac{\partial p}{\partial r} = \frac{v_\theta^2}{r}.$$

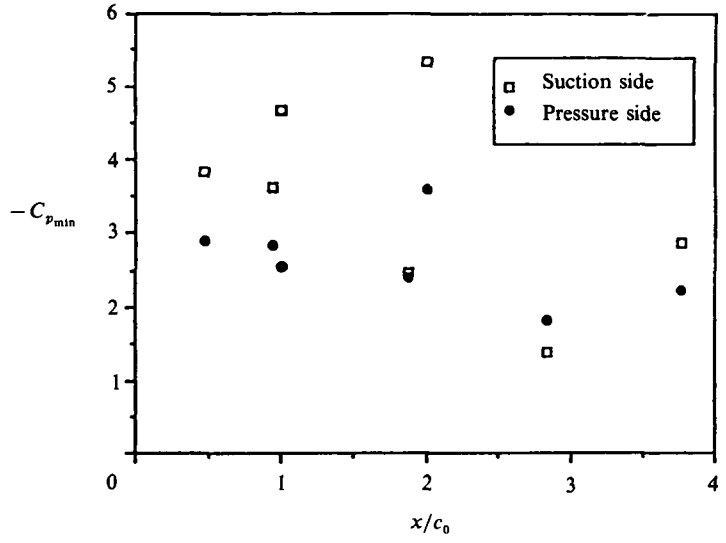

FIGURE 16. Estimate of $C_{p_{min}}$ from velocity measurements $\alpha - \alpha_0 = 12°$, $Re = 5.2 \times 10^5$.

Then, the minimum pressure coefficient at the centre $r = 0$ can be written as

$$C_{p_{min}} = -2 \int_0^\infty \frac{1}{r} \left(\frac{v_\theta}{U_\infty} \right)^2 \mathrm{d}r.$$

Therefore, it is possible to estimate the magnitude of $-C_{p_{min}}$ by the measurement of the tangential velocity field. The velocity profiles are highly asymmetric close to the tip of the hydrofoil, but gradually become symmetric further downstream. The strongly asymmetric profiles are observed for $x/c_0 < 1$, the region from the photograph of figure 1(c) where there is interaction between the primary tip vortex and the secondary vortices. Owing to the observed asymmetries, estimations of $-C_{p_{min}}$ were made separately for the pressure and suction sides. The results are plotted in figure 16.

The magnitude of $-C_{p_{min}}$, estimated in the manner described, varies substantially from suction to pressure side and on both sides it varies with downstream location. The latter is an indication of axial pressure gradients within the core. The σ_i value from figure 7 at the conditions of the velocity measurements is approximately 3.6 which is bracketed by the estimates of $-C_{p_{min}}$ shown in figure 16. The apparent consistency between the pressure calculations and our observations in §3.2 should be viewed with caution. Tension effects were suggestive from definitive experiments like the results shown in figure 8, which would lower σ_i below $-C_{p_{min}}$. However, in addition to the estimated value $-C_{p_{min}}$, we should add a pressure coefficient based on the fluctuating component of the pressure field. Even a rough magnitude of the latter is totally unknown at the present time. The effects of tension and flow unsteadiness are of opposite signs and may partially or fully cancel each other. In addition, we may have to question the validity of estimating $-C_{p_{min}}$ by the techniques used in the presence of strong asymmetric velocity profiles and possibly large axial flow velocities. It should also be pointed out that the values of $-C_{p_{min}}$ for a Rankine vortex or a Lamb vortex with the measured circulation are substantially higher than the values in figure 16. This indicates that the velocity distribution differs substantially from idealized models.

4. Summary

Several observations in relation to cavitation in a tip vortex trailing from a lifting hydrofoil of elliptic planform and moderate aspect ratio have been presented. The real fluid flow past the hydrofoil is observed and predicted to possess a laminar separation bubble at a Reynolds number of 5.3×10^5. Since the local chord Reynolds number of an elliptic planform decreases towards the tip, boundary-layer computations show that a short separation bubble should change over to a long separation bubble near the tip. This can result in a relatively strong secondary vortex downstream of the foil which can interact with the roll-up of the primary vortex sheet. Cavitation observations under developed conditions seem clearly to show the existence of secondary vortices. In addition, detailed probing of the velocity field with LDV show strong asymmetries for downstream distances less than or close to the base chord value. This feature is most likely related to the interactions just noted. The cavitation number associated with tip-vortex cavitation inception show a complex dependence on the Reynolds number and air content value. Some of the observations can be related to tension effects associated with the lack of supply of sufficiently large-sized nuclei for inception. This information has been inferred and is not based on direct nuclei size measurements. The measured asymmetric tangential velocity profiles have been integrated separately on the suction and pressure side to obtain the magnitude of minimum pressure coefficient, at the centre of the vortex core at a given axial location. These magnitudes differ substantially on the suction and pressure side and also on the axial location. The maximum of the negative value of the minimum pressure coefficient obtained in the manner indicated compares favourably with the magnitude of the inception cavitation number for the conditions of the velocity survey. However, the latter is somewhat higher, indicating lack of tension effects, but one cannot come to this conclusion without a knowledge of the fluctuating levels of pressure in tip-vortex flows. This knowledge is completely lacking at the present time. The observed tip-vortex cavity trajectory shows a surprising non-dependence on any of the physical parameters varied, like angle of attack, Reynolds number, cavitation number and dissolved gas content. There are both qualitative and quantitative differences between the observed tip-vortex cavity trajectory and the predicted tip location of the vortex sheet roll-up from numerical analysis of the problem under non-cavitating conditions.

This research was supported by the Office of Naval Research under the SRO Program in Hydroacoustics. M. Rogers, S. Jiang and J. Killen assisted in the experimental work. The authors would like to thank Dr Krasny for making certain original drawings available to them. The first author would like to recognize the support of the Alexander von Humboldt Foundation in the preparation of this manuscript.

REFERENCES

Abbot, I. H. & Doenhoff, A. E. von 1959 *Theory of Wing sections*. Dover.

Arakeri, V. H. 1974 A note on the transition observations on an axisymmetric body and some related fluctuating wall pressure measurements. *Trans. ASME* I: *J. Fluids Engng* **97**, 82–86.

Arakeri, V. H. 1975 Viscous effects on the position of cavitation separation from smooth bodies. *J. Fluid Mech.* **68**, 779–799.

Arakeri, V. H. & Acosta, A. J. 1973 Viscous effects in the inception of cavitation on axisymmetric bodies. *Trans. ASME* I: *J. Fluids Engng* **95**, 519–527.

ARAKERI, V. H., HIGUCHI, H. & ARNDT, R. E. A. 1986 Analysis of recent tip vortex cavitation inception data. In *Proc. 21st Am. Towing Tank Conf., Washington, DC.*

ARAKERI, V. H., HIGUCHI, H. & ARNDT, R. E. A. 1988 A model for predicting tip vortex cavitation characteristics. *Trans. ASME* I: *J. Fluids Engng* 190–193.

ARNDT, R. E. A. & GEORGE, W. K. 1978 Pressure fields and cavitation in turbulent shear flows. In *12th Symp. on Naval Hydrodynamics, Washington, DC.*

ARNDT, R. E. A. & KELLER, A. P. 1976 Free gas content effects on cavitation and noise in a free shear flow. In *Proc. IAHR Symp. on Two Phase Flow and Cavitation in Power Generation Systems, Grenoble.*

BATCHELOR, G. K. 1964 Axial flow in trailing line vortices. *J. Fluid Mech.* **20**, 645–658.

EPSTEIN, P. S. & PLESSET, M. S. 1950 On the stability of gas bubbles in liquid-gas solutions. *J. Chem. Phys.* **18**, 1505–1509.

GASTER, M. 1967 The structure and behaviour of laminar separation bubbles. *NPL Aero Rep.* 1181 (Revised).

HIGUCHI, H., ARNDT, R. E. A., ARAKERI, V. H. & KILLEN, J. M. 1989*a* The structure of tip vortices over a wide range of cavitation number. *Proc. Am. Towing Tank Conf., St. Johns, New Foundland, August.*

HIGUCHI, H., ARNDT, R. E. A. & ROGERS, M. F. 1989*b* Characteristics of tip vortex cavitation noise. *Trans. ASME* I: *J. Fluids Engng* **111**, 495–501.

HIGUCHI, H., QUADRELLI, J. C. & FARELL, C. 1987 Vortex roll-up for an elliptically-loaded wing at moderately low Reynolds number. *IAA J.* **25**, 1537–1542.

KATZ, J. 1984 Cavitation phenomena within regions of flow separation. *J. Fluid Mech.* **140**, 397–436.

KNAPP, R. T., DAILY, J. W. & HAMMITT, F. G. 1970 *Cavitation.* McGraw-Hill.

KRASNY, R. 1987 Computation of vortex sheet roll-up in the Trefftz plane. *J. Fluid Mech.* **184**, 123–155.

MANUEL, F., CRESPO, A. & CASTRO, F. 1987 Wave and cavity propagation along a tip vortex interface. *Physio Chem. Hydrodyn.* **9**, 611–620.

MCCORMICK, B. W. 1962 On cavitation produced by a tip vortex trailing from a lifting surface. *Trans. ASME* D: *J. Basic Engng* **84**, 369–379.

NUHAIT, A. O. & MOOK, D. T. 1988 Numerical simulation of wings in steady and unsteady ground effects. *AIAA Paper* 88-2546-CP.

OOI, K. K. 1985 Scale effects on cavitation inception in submerged water jets; a new look. *J. Fluid Mech.* **151**, 367–390.

SMITH, A. M. O. & GAMBERONI, N. 1956 Transition, pressure gradient and stability theory. *Rep.* ES 26388. Douglas Aircraft Co.

SPALART, P. R. & LEONARD, A. 1981 Computation of separated flows by a vortex algorithm. *AIAA Paper* 81-1246.

STRAUB, L. G., RIPKEN, J. F. & OLSON, R. M. 1955 The six-inch water tunnel at the St. Anthony Falls Hydraulic Laboratory and its experimental use in cavitation studies. In *NPL Sympon. Cavitation in Hydrodynamics, Teddington, UK.* (Available as *SAFHL Tech Paper* 16-B, 1956.)

WAZZAN, A. R., OKAMURA, X. X. & SMITH, A. M. O. 1968 Spatial and temporal stability charts for the Falkner–Skan boundary layer profiles. *Rep.* DAC 67086. McDonnell Douglas Corp.

WETZEL, J. M. & KILLEN, J. M. 1982 The St. Anthony Falls Hydraulic Laboratory high speed, variable pressure, free surface flow facility. In *Proc. 22nd NATO Defense Research Group Seminar on Advanced Hydrodynamic Testing Facilities, The Hague, Netherlands.*